RSC Advances

PAPER

View Article Online
View Journal | View Issue

Cite this: *RSC Adv.*, 2021, **11**, 14504

Studies on structural, dielectric and optical properties of $(Ba_{0.95}Ca_{0.05})_{1-x}(Ti_{0.8}Sn_{0.2})_{1-x}Na_xNb_xO_3$ lead-free ceramics

H. Slimi, *[a] A. Oueslati [b] and A. Aydi[a]

Received 4th February 2021
Accepted 4th April 2021

DOI: 10.1039/d1ra00952d

rsc.li/rsc-advances

$(Ba_{0.95}Ca_{0.05})_{1-x}(Ti_{0.8}Sn_{0.2})_{1-x}Na_xNb_xO_3$ (BCNTSNO$_3$) lead-free ceramics with compositions (x = 0.75, 0.8 and 0.85) were synthesized through the traditional solid-state reaction method. X-ray powder diffraction analysis showed the formation of a single phase compound crystallized in tetragonal space group *P4mm*. The evolution of Raman spectra displayed a disorder introduced into the structure, which favors a ferroelectric relaxor behavior. The dependence of the dielectric properties on temperature exhibited two composition ranges with different behaviors. Ferroelectric relaxor properties were observed for the compositions x < 0.85 and the classical ferroelectric behavior for x = 0.85. Lead free $(Ba_{0.95}Ca_{0.05})_{1-x}(Ti_{0.8}Sn_{0.2})_{1-x}Na_xNb_xO_3$ ceramics exhibited larger dielectric constants than those of parent crystal $NaNbO_3$, suggesting that it is a good candidate for lead-free ceramics in several industrial applications. Using UV-Vis spectroscopy, the optical band gap energy of ceramics $(Ba_{0.95}Ca_{0.05})_{1-x}(Ti_{0.8}Sn_{0.2})_{1-x}Na_xNb_xO_3$ is found at 2.89, 2.92, and 3.05 eV for x = 0.75, 0.8 and 0.85, respectively.

1. Introduction

With the recent growing demand for global environmental protection and sustainable development, researchers' interests have turned to lead-free materials such as ferroelectrics with the ABO_3 perovskite structure.[1–3] Due to their multifunctional properties,[4–6] good thermal resistance as well as chemical stability, nature-friendly ferroelectrics may be good candidates for industrial applications. These materials have similar or better physico-chemical properties than toxic ferroelectrics. Ferroelectrics are typical materials that exhibit spontaneous polarization, in which their direction is reversed by reversing the external electric field. However, based on their behavior, ferroelectric materials have been extensively used in multiple fields including multilayer capacitors, electromechanical systems, energy storage and ultrasonic transducers.[7–11] Recently, the coupling of ferroelectric polarization with light absorption makes the ferroelectric perovskites promising candidates for applications in photoelectrics.[12]

Barium titanate ($BaTiO_3$) is a classical ferroelectric used for the preparation of ceramics, which is widely explored given its excellent electrical, dielectric and ferroelectric properties. From the viewpoint of the nature of ferroelectric phase transitions between order-disorder and displacive scenarios, it presents a very large optical band gap energy of about 3.26 eV.[13] In attempts to improve the properties of $BaTiO_3$, dopants are generally added to the A and/or B sites of the material. In this case, the $BaTiO_3$–$CaTiO_3$–$BaSnO_3$ ternary system was studied.[14] The latter may display multiphase coexistence at room temperature such as a Morphotropic phase boundary (MPB) or polymorphic phase boundary (PPB), where good piezoelectric property is expected with a high value of T_C.

Sodium niobate $NaNbO_3$ (NN) is an antiferroelectric (AFE) perovskite with an orthorhombic structure in space group *Pbma* at room temperature.[15] It has attracted attention owing to its successive phases structure transition.[16] In addition, $NaNbO_3$ perovskite is an important photocatalysis semiconductor with a band gap energy of 3.4 eV.[17,18] As a result, NN is also a promising candidate in many areas of optical applications involving energy storage, optical waveguides, ultrafast optical switching, non-volatile ferroelectric memories and semiconductor photoélectrodes.[19] Moreover, in the field of photocatalysis, it is used for the separation of water, purifying the air and the decomposition of dyes.[20,21] Furthermore, the dielectric behavior of NN has been widely investigated. It exhibits a phase transition at T_C around 913 K with a maximum real permittivity of ε'_{rmax} 1750 at T_C.[22] $NaNbO_3$ (NN) is a anti-ferroelectric at room temperature[17] and it transforms to ferroelectric substance, if mixed with a small amount of $KNbO_3$,[7] $LiNbO_3$,[23] $BaSnO_3$,[24] and $SrSnO_3$.[25] However, only several studies have been conducted on the ceramics formed $BaTiO_3$–$NaNbO_3$ system with the aim to examine the effect of cation substitution in

[a]*Laboratory of Multifunctional Materials and Applications (LaMMA), LR16ES18, Faculty of Sciences of Sfax, University of Sfax, BP 1171, 3000 Sfax, Tunisia. E-mail: slimi.houda1@gmail.com*

[b]*Laboratory of Spectroscopic Characterization and Optic Materials, University of Sfax, Faculty of Sciences of Sfax, B.P. 1171, 3000 Sfax, Tunisia*

A and B sites, including significant changes in the dielectric and structural properties.

The mixture or solid solution of anti-ferroelectric and ferroelectric materials usually results in the formation of multifunctional material having good ferroelectric and piezoelectric properties.[26] In this study, antiferroelectric NN and ferroelectric ternary systems $BaTiO_3$–$CaTiO_3$–$BaSnO_3$ are synthesized to develop a new lead free ferroelectric solid solution with general composition $(1 - x)[(Ba_{0.95}Ca_{0.05})(Ti_{0.8}Sn_{0.2})]$ $Na_xNb_xO_3$. The ceramics $(Ba_{0.95}Ca_{0.05})_{1-x}(Ti_{0.8}Sn_{0.2})_{1-x}Na_xNb_xO_3$ with $x = 0.75$, 0.8 and 0.85 were synthesized by means of the conventional solid-state reaction method. The structural and physical properties were explored by X-ray diffraction, dielectric measurements and Raman spectroscopy. The optical properties under UV-visible irradiation were reported.

2. Experimental details

The compounds $(Ba_{0.95}Ca_{0.05})_{1-x}(Ti_{0.8}Sn_{0.2})_{1-x}Na_xNb_xO_3$, ($x$ = 0.75, 0.8 and 0.85), were prepared through the conventional solid-state reaction method. The used precursors are as follows: carbonates ($BaCO_3$, $CaCO_3$ and Na_2CO_3) and oxides (SnO_2, TiO_2 and Nb_2O_5) with 99.9% purity of Aldrich brand. The mixed powders are milled in an agate mortar for 1 hour to homogenize the mixture and reduce the size of the grain size. The homogenized powders are calcined between 1000 and 1100 °C for 12 h in an electric furnace to evaporate CO_2. The calcined powders are ground, again for 1 h and then shaped into pellets of 8 mm in diameter and 1 mm thick to undergo second heat treatment (sintering) at a higher temperature ranging between 1250 and 1400 °C for 2 h.

To examine the phase purity and evolution of the crystal symmetry of the prepared ceramics, the X-ray diffraction measurements were carried out on sintered pellets at room temperature. The intensity determining was performed by a step of 0.02 in 2θ and a counting time of 10 s by means of a Philips X'pert PW 3040/00 diffractometer using the Kα radiation ($\lambda = 1.5406$ Å). Cell parameters and line profile were refined by a global method using the Fullprof program based on Rietveld method.[27]

The dielectric study was carried out on sintered pellets of diameter 7 mm and thickness 1 mm. The impedance spectroscopy measurements were performed as a function of temperature (50–600 K) and frequency (0.1 Hz to 200 kHz) using a Wayne-Kerr 6425 component analyzer.

The Raman spectra were recorded in the wavenumber range of 50–1000 cm^{-1} on a Horiba Lab-ram HR 800 Raman spectrometer equipped with a He–Ne laser of 633 nm emission line with the power of 15 mW and a CCD detector.

The linear optical properties were measured at room temperature, using a UV-3101PC scanning spectrophotometer in the 200–1000 nm wavelength range.

3. Results and discussion

3.1 X-ray diffraction analysis

The X-ray patterns of $(Ba_{0.95}Ca_{0.05})_{1-x}Na_x(Ti_{0.8}Sn_{0.2})_{1-x}Nb_xO_3$ ceramics of compositions ($x = 0.75$, 0.8 and 0.85) indicate that all the samples have pure perovskite-type structures without secondary phases, implying that the Ba^{2+}, Ca^{2+}, Sn^{4+}, and Ti^{4+} ions are well incorporated on the A and B sites of $NaNbO_3$ lattice. The Rietveld refinements of the XRD patterns exhibit a tetragonal phase with space group *P4mm* at room temperature. This symmetry is characterized by a (002)/(200) peak splitting between 45° and 46°. As an example, the difference diffraction pattern for $x = 0.75$ is shown in Fig. 1.

The corresponding results and the estimated values of the refinement parameters of the title ceramics are summarized in Table 1. One can notice that, when x increases, the cell parameters a, b, c and cell volume v increase. These results can be related to the increase of the ionic radii of the cations substituted in A and B sites.

The values of the ionic radii $(r_{Na^+}) = 1.18$ Å and $(r_{Nb^{5+}}) = 0.64$ Å coordinated with 8 and 6 respectively for NN lower than those of $(r_{Ba^{2+}}) = 1.61$ Å, $(r_{Ca^{2+}}) = 1$ Å, $(r_{Sn^{4+}}) = 0.69$ Å and $(r_{Ti^{4+}}) = 0.605$ Å in coordination with 6 in BTS.[28] Moreover, these results are in relation with the variations of the average radii in site A $\langle r_A \rangle$ and in site B $\langle r_B \rangle$. The following relations govern these radii:

$$\langle r_A \rangle = x(r_{Na^+}) + (1 - x)[0.95(r_{Ba^{2+}}) + 0.05(r_{Ca^{2+}})]$$

$$\langle r_B \rangle = x(r_{Nb^{5+}}) + (1 - x)[0.8(r_{Ti^{4+}}) + 0.2(r_{Sn^{4+}})]$$

According to the calculations, we notice that the ionic radius $\langle r_A \rangle$ decreases from 1.27 to 1.239 Å, respectively, for $x = 0.75$ and 0.85. As it appears, in this case, the ionic radius in A site should increase. However, the ionic radius $\langle r_B \rangle$ of the B-site increases with a small step from 0.635 to 0.638 Å. Therefore, the increase of the lattice parameters as well as the cell volume as a function of compositions could be accounted for in terms of the increase of $\langle r_B \rangle$ rather than $\langle r_A \rangle$.

It is interesting to find out the regularities, which govern the formation of perovskite compounds and use them to further guide the exploration of new materials. In the early 1920s, Goldschmidt[29] proposed a tolerance factor "t" to study the stability of perovskite, defined as:

$$t = \frac{r_A + r_O}{\sqrt{2}(r_B + r_O)} \quad (1)$$

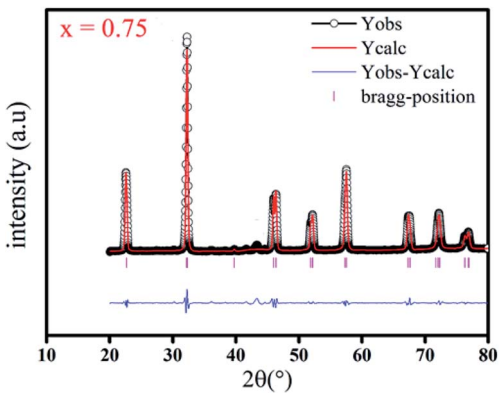

Fig. 1 X-ray diffraction pattern at room temperature of BCNTSNO ceramic with composition corresponding to $x = 0.75$.

Table 1 The refinement results of X-ray pattern and cell parameters of $(Ba_{0.95}Ca_{0.05})_{1-x}Na_x(Ti_{0.8}Sn_{0.2})_{1-x}Nb_xO_3$ with different structure

$(Ba_{0.95}Ca_{0.05})_{1-x}Na_x(Ti_{0.8}Sn_{0.2})_{1-x}Nb_xO_3$	$X = 0.75$	$X = 0.8$	$X = 0.85$
Phase	Tetragonal	Tetragonal	Tetragonal
Space group	*P4mm*	*P4mm*	*P4mm*
Lattice parameters	$a = b = 3.916$ Å	$a = b = 3.919$ Å	$a = b = 3.924$ Å
	$c = 3.946$ Å	$c = 3.9447$ Å	$c = 3.945$ Å
	$v = 60.498$ Å^3	$v = 60.567$ Å^3	$v = 60.685$ Å^3
$\langle r_A \rangle$	1.279	1.259	1.239
$\langle r_B \rangle$	0.635	0.637	0.638
t	0.924	0.917	0.910

where, r_A, r_B and r_O are ionic radii of A-site cation, B-site cation and oxygen, respectively. In general, the perovskite structure is stable for t values obeying $0.75 < t < 1.06$ and the symmetry is high as long as the t value is close to 1. This parameter is suggestive of how far the atoms can move from the ideal packing and be still belonging to the perovskite structure. The tolerance factor was calculated in the order of $t = 0.9$, which is plotted in Table 1. Hence, we can deduce that the structure of all the ceramics is stable.

3.2 Raman spectroscopy

The Raman spectra of the BCNTSNO ceramics at various compositions ($x = 0.75$, 0.8 and 0.85) at room temperature, were measured to further explore the evolution of the structure of BCNTSNO ceramics, as shown in Fig. 2.

The presence of three mains regions, which are detected in the parent compounds $BaTiO_3$ and $NaNbO_3$ is evident in Fig. 2.[30,31] The region (I), the modes at wavenumbers <170 cm^{-1} is associated with external vibrations of NbO_6 octahedron, which is connected to the vibrations of the perovskite A-site). The region (II), the 170–450 cm^{-1} modes related to O–Nb–O bending; zone (III), the 450–800 cm^{-1} host modes related to the NbO_6 octahedral vibrations. These two regions are attributed to the internal vibration of the NbO_6 octahedron. To get the accurate change affected in the position, intensity and half-width of all bands with the increasing of x, Raman spectra are fitting with Fityk program, using pseudo-Voigt function. An example of the Raman spectrum fitting for $x = 0.75$ in the 50–1000 cm^{-1} spectral range is given in Fig. 3. The assignments of principal bands are reported in Table 2.

The bands situated between 60–101 cm^{-1} are related to Na^+ translational movements, while the vibrational band located at 144 cm^{-1} is associated with the Ba^{2+} stretching vibration.[32] A small shift in the intensity and frequency is observed for these bands with increasing composition x.

Accordingly, the Raman modes observed at approximately 177 and 263 cm^{-1} are attributed to the ν_6 and ν_5 modes, respectively, which are in turn assigned to the (Nb–O) bending vibration of the NbO_6 octahedra. Moreover, the existence of the mode $B_1 + E(TO + LO)$ around 326 cm^{-1} confirmed the presence of the tetragonal phase in all ceramics, as was detected by XRD studies.[33] The band detected at 434 cm^{-1} is related to asymmetric bending vibration ν_4(Nb–O).[25] However, the intense Raman band of the prepared lead-free ceramics in the 598–606 cm^{-1} region corresponds to a shoulder in the 551–561 cm^{-1} region. These bands ν_1 are and ν_2 are assigned to symmetric and asymmetric stretching modes of the NbO_6 octahedra. Finally, the mode at 863 cm^{-1} is attributed to $\nu_1 + \nu_5$ vibration modes combination, associated with the Sn–O stretching vibration.[31] A most significant change is observed in the characteristics of the internal bands on increasing the degree of substitution, except

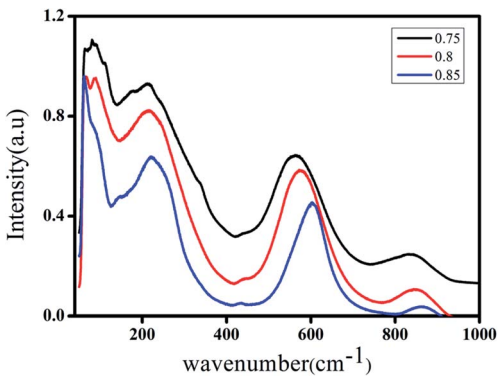

Fig. 2 Room temperature Raman spectra of $(Ba_{0.95}Ca_{0.05})_{1-x}Na_x(Ti_{0.8}Sn_{0.2})_{1-x}Nb_xO_3$ ceramics with $x = 0.75$, 0.8 and 0.85 compositions.

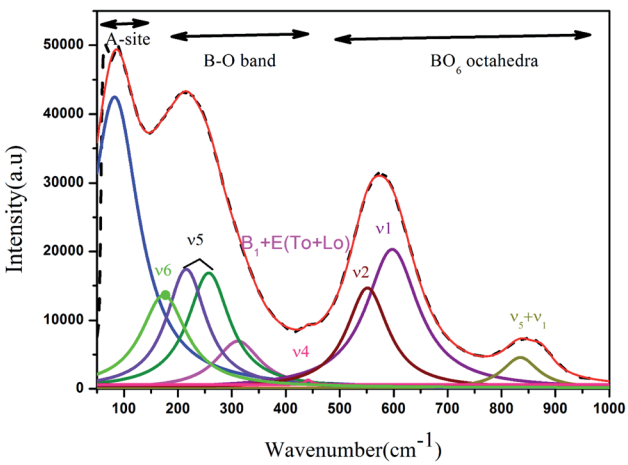

Fig. 3 Deconvolution of Raman spectra of the $BCNTSNO_{0.75}$ ceramic at room temperature.

Table 2 Wavenumbers of the Raman modes and their assignments

		Assignments			
$NaNbO_3$ (ref. 31)	$Ba_{0.1}(Sn_{0.5}Ti_{0.5})_{0.1}Na_{0.9}Nb_{0.9}O_3$ (ref. 34)	$x = 0.75$	$x = 0.8$	$x = 0.85$	
64	62	60	60.0	61	Na^+
—	—	66	66	66	Na^+
76	—	70	71	75	Na^+
—	—	—	—	—	
95	—	—	84	—	
—	—	99	100	101	Na^+
126	105	—	—	—	
	—	—	—		
146					
—	—	143	145	144	Ba^{2+}
157	154	—	—	—	
—	—	—		—	
180	—	173	174	177	ν_6 (Nb–O)
—	—	—	—	—	
186	—	—	—	—	
—	—				
223	222	215	214	219	ν_5 (Nb–O)
258	240	257	262	263	
279	275	—	—	—	
375	—	311	324	326	E(TO + LO)
433	430	441	445	434	ν_4 (Nb–O)
560	—	551	552	561	ν_2 (Nb–O)
				—	
605	601	598	601	606	ν_1 (Nb–O)
	867	835	849	863	$\nu_1 + \nu_5$(Sn–O)

for the increased splitting and shifting of the peak on the right side to higher frequencies. Also, we notice that these bands become more broadening with the increase of the composition x, which implied that the internal mode was sensitive to the effect of substitution in the $NaNbO_3$.

Additionally, it can also be seen from the Raman spectra that with incasing the composition x, no peaks are observed indicating the absence of formation of a new phase and consequently the formation of solid solutions, which confirms the results found by DRX. When the composition x increases, all the bands display a decreasing intensity and shifted to the high frequency. This behavior can be connected with the disorder of ionic charge created on the A and B sites of $NaNbO_3$ and distortion of NbO_6 octahedra, as a consequence of Ba, Ca, Sn, and Ti substitutions.

3.3 Dielectric study

The dependence of relative permittivity (ε'_r) of $(Ba_{0.95}Ca_{0.05})_{1-x}(Ti_{0.8}Sn_{0.2})_{1-x}Na_xNb_xO_3$ ceramics for $x = 0.75$, 0.8 and 0.85 on temperature at some particular frequencies is illustrated in Fig. 4a and b. The dielectric characterization of the prepared ceramics shows an evolution from relaxor ferroelectric behavior to a classic ferroelectric under the effect of the degree of substitution of the cation Na^{2+} by (Ba^{2+}, Ca^{2+}) and Nb^{5+} by (Ti^{4+}, Sn^{4+}) in A and B sites, respectively. Meanwhile, for all the prepared lead-free ceramics a signal dielectric peak is observed, corresponding to ferroelectric paraelectric transition.

For the compositions $x < 0.85$ (Fig. 4a), when the frequency increases, the temperature of the maximum of the real part ε'_{rmax} note T_m moves towards the highest temperatures, whereas the magnitude of permittivity decreases. As a result, large dispersion is observed around and below T_m as a function of frequency in all samples, strongly resembling the behavior in relaxor ferroelectrics.[34] The homovalents and heterovalents substitutions at sites A and B for our ceramics and the composition fluctuation, give rise to the relaxing behavior, and thus favoring the strong heterogeneity of the composition with various Curie points.[35] Furthermore, the creation of the Coulomb interactions at long-distance prevents the formation of ferroelectric microdomains in favor of the formation of the polar nanoregions PNRs.[36] Under these conditions, the order becomes a short distance and each nano-domain freeze at a given temperature. This phenomenon only demonstrates the nature of the transition, whereas the dielectric relaxation observed for temperatures lower than T_m remains unjustified. This dielectric dispersion is explained by the dynamics of the nano-domains.[37] The relaxor characteristics of compositions $x = 0.75$ and 0.8 are depicted in Table 3.

For $x \geq 0.85$ (Fig. 4b), the maximum value of the real part ε'_{rmax} decreases with the increase in the frequency but the temperature of Curie (T_C) remains constant, which justifies the classical ferroelectric behavior of the ceramics.

From the Fig. 4, it could be seen that when x increases from 0.75 to 0.8 and 0.85 the values of the maximum dielectric

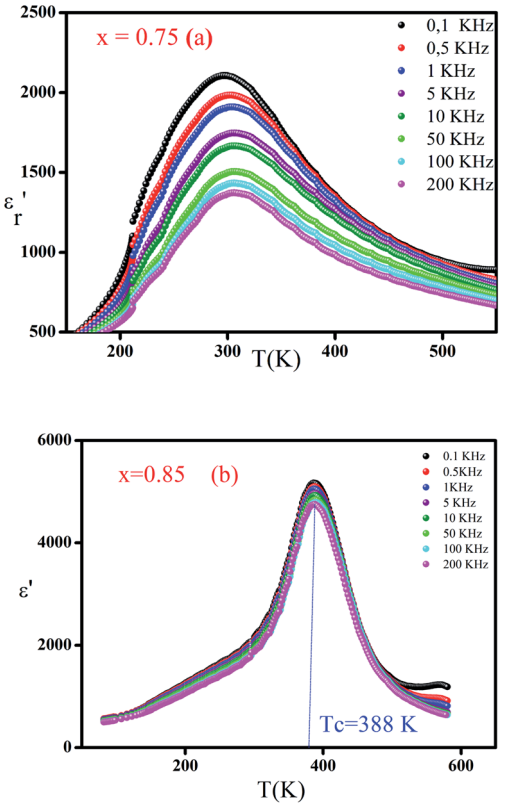

Fig. 4 Thermal variation of the real part (ε'_r) of the dielectric permittivity of $(Ba_{0.95}Ca_{0.05})_{1-x}Na_x(Ti_{0.8}Sn_{0.2})_{1-x}Nb_xO_3$ with compositions at different frequencies (a) $x = 0.75$ and (b) $x = 0.85$.

constant of $(Ba_{0.95}Ca_{0.05})_{1-x}(Ti_{0.8}Sn_{0.2})_{1-x}Na_xNb_xO_3$ ceramics increases gradually from 2106 to 4421 and 5224. This maximum is higher than the value of the pure NN ($\varepsilon'_{rmax} = 1750$),[13] suggested that the introduction of Ba, Ca, Sn and Ti at A and B sites can increase the maximum of the dielectric constant, which is can be caused by the grain size effect.

Additionally, it is worth noting that the temperature of ferroelectric to paraelectric transition shifted to higher temperature from 298 K to 320 K and 388 K, which are mostly smaller than the transition temperature of the NN ($T_C = 913$ K)[20,22] and the dielectric peak at this temperature becomes less broadened with increasing level x. These results display that the substation in the A and B sites of $NaNbO_3$ induced that the $(Ba_{0.95}Ca_{0.05})_{1-x}(Ti_{0.8}Sn_{0.2})_{1-x}Na_xNb_xO_3$ ceramic transformed from a relaxor ferroelectric to a classical ferroelectric.

Table 3 Values of factor: ε'_{rmax}, T_m, ΔT_m, $\frac{\Delta\varepsilon'_r}{\varepsilon'_r}$ and γ for the compositions $x = 0.75$ and $x = 0.8$ of $(Ba_{0.95}Ca_{0.05})_{1-x}Na_x(Ti_{0.8}Sn_{0.2})_{1-x}Nb_xO_3$

x	ε'_{rmax} (10 kHz)	T_m (K) (10 kHz)	ΔT_m (K)	T_{dev} (K)	$\frac{\Delta\varepsilon'_r}{\varepsilon'_r}$	γ
0.75	1666	308	8	376	0.40	1.87
0.8	4148	324	6	404	0.10	2

In this context, departing from the dielectric results we infer that a substitution level of Ba, Ca, Sn and Ti modify the $NaNbO_3$ ceramic from antiferroelectric behavior to ferroelectric behavior, showing an important enhancement important of the dielectric constant, with a decrease of the Curie temperature around room temperature. Comparing, our results with the pure $NaNbO_3$, it is obvious that the studied ferroelectric ceramics with high dielectric permittivity around room temperature show interesting as a potential candidate for lead-free ceramics in several industrial applications such as for non-volatile random access memory technology information storage in electronic devices.

Fig. 5a and b show the thermal evolution of the imaginary part of the permittivity and the dielectric loss for a classical ferroelectric ceramic with composition $x = 0.85$ as an example. We may notice that the dielectric losses are about 5%.

Moreover, for a normal ferroelectric, the thermal evolution of dielectric constant above the Curie temperature in the paraelectric region is described by a Curie–Weiss law equation:

$$\varepsilon'_r = \frac{c}{(T - T_C)} \quad T > T_C \tag{2}$$

where T_C refers to the Curie temperature and c to the Curie–Weiss constant.

Fig. 6a and b, disclose as an example the thermal evolution of the inverse of (ε'_r) at 10 kHz for $x = 0.75$ (relaxor) and 0.85 (classical), respectively. The fits to the experimental data are obtained by eqn (2). The relaxor ceramics $x = 0.75$, (ε'_r) presents

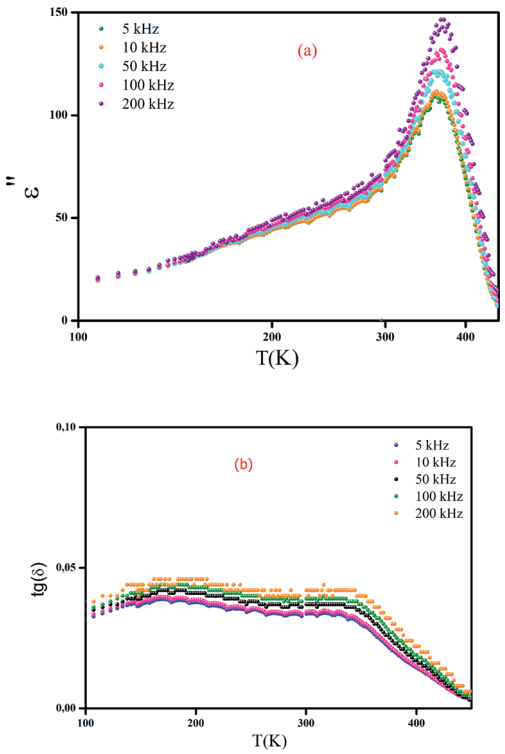

Fig. 5 Thermal evolution of the imaginary part of the permittivity (a) and dielectric loss (b) for $(Ba_{0.95}Ca_{0.05})_{1-x}Na_x(Ti_{0.8}Sn_{0.2})_{1-x}Nb_xO_3$ ceramics with $x = 0.85$.

a deviation from the Curie–Weiss law at a deviation temperature T_{dev} that is defined as the temperature from which it starts to deviate from the Curie–Weiss law. However, the evolution of the inverse of constant dielectric for $x = 0.85$ obeys the Curie Weiss law implying that the transition from the paraelectric phase to the ferroelectric phase is clearly of the second order and the ferro-electricity is of classical type.[38]

Modified Curie law by Uchino and Nomura is used to describe the dielectric relaxation behavior of the $(Ba_{0.95}Ca_{0.05})_{1-x}(Ti_{0.8}Sn_{0.2})_{1-x}Na_xNb_xO_3$ ceramics. Generally, the modified Curie–Weiss law can be described by the following equation described as.[39]

$$\frac{1}{\varepsilon'_r} - \frac{1}{\varepsilon'_{rmax}} = c(T - T_m)^{\gamma} \quad (3)$$

where c denotes the Curie constant and $1 < \gamma < 2$ is defined as the diffuseness degree indicator of the character of the phase transition.[40] Linear relationships are observed in the plot of $\log\left(\frac{1}{\varepsilon'_r} - \frac{1}{\varepsilon'_{rmax}}\right)$ as a function of $\log(T - Tm)$ at 10 kHz frequency for the compositions $x = 0.75$ and $x = 0.8$ as shown in (Fig. 7a and b). The slope of linear fitting the experimental data to eqn (3) allows determining the values of γ diffusion factor, as listed in Table 3. We observe that the values of γ increase monotonously with the increasing x, indicating a shift toward more diffusive phase transition.[41] These results are in good agreement with those reported in the prototype relaxor $PbMg_{1/3}Nb_{2/3}O_3$, 1.6 (ref. 42) and $Na_{1-x}Sr_x(Sn_{0.25}Ti_{0.75})_xNb_{1-x}O_3$ lead-free[43] ceramic.

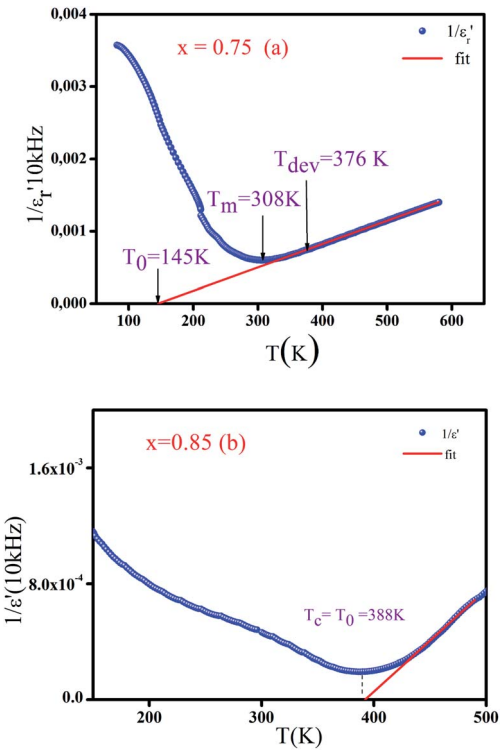

Fig. 6 Variation of the inverse of the real part of the dielectrique permittivity *versus* temperature for BCNTSN: (a) $x = 0.75$ and (b) $x = 0.85$ ceramics.

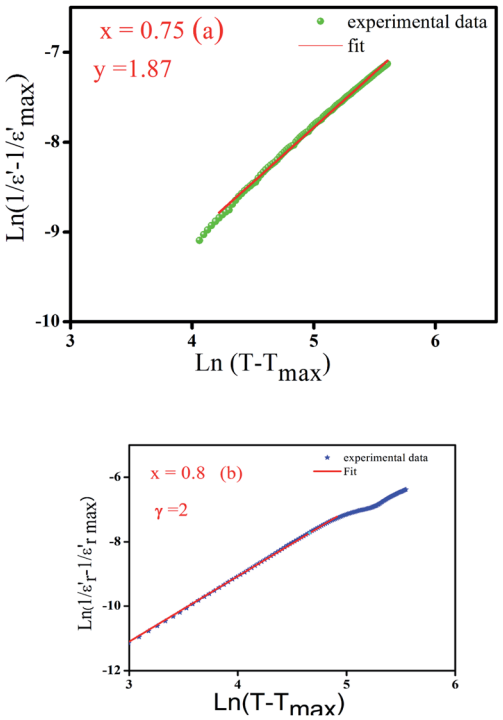

Fig. 7 Variation of $\ln(1/\varepsilon'_r - 1/\varepsilon'_{rmax})$ as a function of $\ln(T - T_{max})$ at 10 kHz of (a) $x = 0.75$ and (b) $x = 0.8$ of $(Ba_{0.95}Ca_{0.05})_{1-x}Na_x(Ti_{0.8}Sn_{0.2})_{1-x}Nb_xO_3$ ceramics.

3.4. Optical properties

The absorbance spectra of all compounds at room temperature in the wavelength range (200–1000 nm) are plotted in Fig. 8. We noticed a decrease of the absorption with the increase of wavelengths whose characteristic peaks are shifted towards smaller wavelengths with the increase in $NaNbO_3$ content, indicating a blue shift, which is suggestive of the increase in the band gap.[44] This corresponds to a typical behavior for numerous semiconductors and can refer to many reasons such as internal electric fields within the crystal and inelastic scattering of charge carriers by phonons.[45] Furthermore, this behavior may be attributed to the quantum confinement arising from the lowering of particle size.[46]

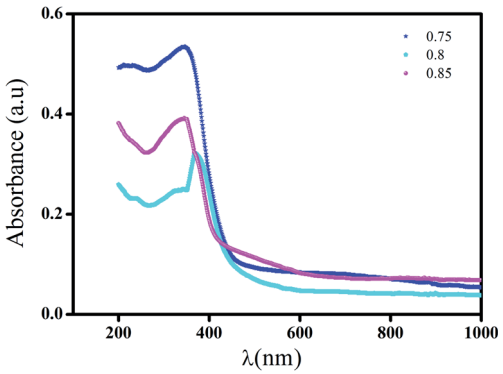

Fig. 8 Variation of absorbance at room temperature.

These compounds absorb in the UV-visible region with the same order of absorption bands. These bands can be attributed to the inter-band transition which is formed by the 4d orbitals of NbO_6 (bottom of conduction band) to 2p orbitals of O_2 (top of valence band). The band in the region $\lambda \geq 400$ nm can be associated with an interband transition in relation to the Nb^{5+} cation.[18,47]

3.5 Optical band gap and Urbach energies

The optical band gap energy (E_g) values of $(Ba_{0.95}Ca_{0.05})_{1-x}Na_x(Ti_{0.8}Sn_{0.2})_{1-x}Nb_xO_3$ ceramics are determined using the Kubelka–Munk model as:[48]

$$F(R) = \frac{1-R^2}{2R} \quad (4)$$

where $F(R)$ is the Kubelka–Munk function and R is the reflectance of the sample. The absorption coefficient (α) is calculated by using the Kubelka–Munk function in terms of:

$$\alpha = \frac{F(R)}{t} \quad (5)$$

where t is the width of the sample.

The relation used for the determination of the optical band energy is the following:

$$\alpha h\nu = \mathrm{B}(h\nu - E_g)^n \quad (6)$$

where B is a constant and $h\nu$ is the photon energy calculated using the equation:

$$h\nu = \frac{1240}{\lambda\ (\mathrm{nm})}$$

The value of n depends on the nature of the electronic transition responsible for absorption. It is equal to 1/2 and 3/2 for allowed and forbidden direct transitions respectively and to 2 and 3 for allowed and forbidden indirect transitions respectively.[49] Since the perovskite suffers from allowed direct transition, the value of the index n is assumed to be 1/2.[25]

Fig. 9 highlights the plot of $(\alpha h\nu)^2$ *versus* $(h\nu)$ of all samples. By extrapolating the linear part of the curve to the x-axis; we determine the value of direct band gap energy E_g.

Table 4 Calculated values of optical band gap (E_g), Urbach energy (E_U) and Cauchy parameter for BCNTSNO ceramics with composition corresponding to $x = 0.75$, 0.8 and 0.85

$(Ba_{0.95}Ca_{0.05}Ti_{0.8}Sn_{0.2})_{1-x}Na_xNb_xO_3$	E_g (eV)	E_U (eV)
0.75	2.89	0.348
0.8	2.92	0.350
0.85	3.05	0.375

The calculated values of the optical band gap of the $(Ba_{0.95}Ca_{0.05})_{1-x}Na_x(Ti_{0.8}Sn_{0.2})_{1-x}Nb_xO_3$ ceramics are found to be 2.89, 2.92 and 3.05 eV for $x = 0.75$, 0.8 and 0.85, respectively, these values are portrayed in Table 4. Obviously, a little blue shift of the optical band gap occurs when the $NaNbO_3$ content increases, as the pure NN presents a large band gap (E_g = 3.4 eV). This phenomenon may be caused by the Burstein–Moss effect.[50] Furthermore, we can notice that the band gap of our ceramics is smaller than that of $NaNbO_3$. This difference can be assigned to the effect of the degree of substitution of the cation Na^{2+} by (Ba^{2+}, Ca^{2+}) and Nb^{5+} by (Ti^{4+}, Sn^{4+}) in A and B sites, respectively, which are expected to perturb the electronic structure of the system.

The narrower band gap might be assigned to an increase in unit cell volume as it can result in a distortion of the unit cell and therefore can produce a decrease in the overlap between O-2p and metal (d) states.[51] The forbidden band of ceramics $(Ba_{0.95}Ca_{0.05})_{1-x}Na_x(Ti_{0.8}Sn_{0.2})_{1-x}Nb_xO_3$ in the order of 3.00 eV, may be useful in photocatalytic and solar cell applications.

The Urbach energy (E_U), corresponds to the degree of disorder in the material characterizing the local defects. It can be calculated from the following equation:[52]

$$\alpha(h\nu) = \alpha_0 \exp\left(\frac{h\nu}{E_U}\right) \quad (7)$$

where α_0 is a constant, $h\nu$ is the photon energy and E_U is the Urbach energy. Taking the logarithm of the two sides of the above equation:

$$\ln(\alpha) = \ln(\alpha_0) + \frac{h\nu}{E_U} \quad (8)$$

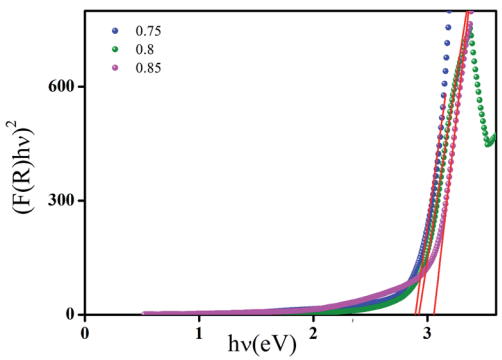

Fig. 9 Plots of $(\alpha h\nu)^2$ *versus* photon energy ($h\nu$ (eV)) for $(Ba_{0.95}Ca_{0.05})_{1-x}Na_x(Ti_{0.8}Sn_{0.2})_{1-x}Nb_xO_3$ ceramics with $x = 0.75$, 0.8 and 0.85 compositions.

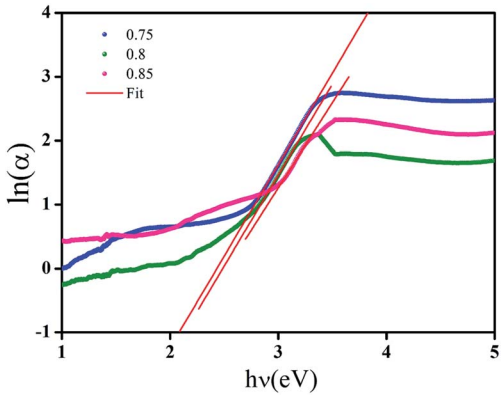

Fig. 10 Plots of ln α *versus* photon energy ($h\nu$) of BCNTSNO ceramics with $x = 0.75$, 0.8 and 0.85 compositions.

The values of Urbach energy (E_U) can be, therefore, obtained from the slope of the straight line of plotting $\ln(\alpha)$ against the incident photon energy ($h\nu$) Fig. 10. The values of the Urbach energy (E_U) of $(Ba_{0.95}Ca_{0.05})_{1-x}Na_x(Ti_{0.8}Sn_{0.2})_{1-x}Nb_xO_3$ ceramics with $x = 0.75$, 0.8 and 0.85, are respectively 0.348, 0.350 and 0.375 eV (Table 4). It is worth noting that the Urbach energy increases when the $NaNbO_3$ content increases. As this energy is associated with the microstructural disorder of the network, it can be suggested that the increase in $NaNbO_3$ content leads to an increase in the number of disorders of our ceramics.

4. Conclusions

Lead free ceramics $(Ba_{0.95}Ca_{0.05})_{1-x}(Ti_{0.8}Sn_{0.2})_{1-x}Na_xNb_xO_3$ ($x =$ 0.75, 0.8 and 0.85), prepared by the conventional solid-solid reaction method, is crystallized in tetragonal structure with space group *P4mm*. Lattice parameters increase with increasing $NaNbO_3$ concentration. These results can be related to the increase of the ionic radii of the substituted cations.

The Raman spectroscopy exhibits a disorder introduced into this composition, which is related to the internal modes of the NbO_6 group, and implied that the internal mode was sensitive to the effect of substitution. As a result, this disorder favors a ferroelectric relaxor behavior. The temperature dependence of the dielectric properties of the prepared ceramics reveals that a doping level of Ba, Ca, Sn and Ti modify the $NaNbO_3$ ceramics from antiferroelectric to ferroelectric, implying a decrease in the Curie temperature, with an increase of the dielectric constant. Moreover, the dependence of the dielectric properties on temperature exhibited two behavior a relaxor behavior for the compositions $x = 0.75$ and 0.8 and a classical ferroelectric behavior for the compositions $x = 0.85$. The enhancement of the dielectric properties of the $NaNbO_3$ was marked by the shift of the curie temperature to room temperature and the increase of the maxim of permittivity due to (Ba^{2+}, Ca^{2+}) and (Ti^{4+}, Sn^{4+}) substitutions.

Finally, UV-Vis spectra disclose that all lead-free ceramics absorb in the UV-visible region with a blue shift in wavelength along with an increase in $NaNbO_3$ concentration. The Tauc model is used to determine the optical gap energy. The analysis of data indicates the existence of optical indirect gaps, estimated to be in the order of 3 eV, which is much smaller than that $NaNbO_3$ ceramic. Therefore, the improvement of the dielectric and optical properties makes our lead-free ferroelectric material suitable for device memory, in photocatalytic and in solar cell applications.

As perspectives for this work, we can consider making the ferroelectric polarization (*P–E*) hysteresis and the electrical measurements.

Conflicts of interest

The authors declare that they have no known competing financial interests or personal relationships that could have appeared to influence the work reported in this paper.

The authors declare the following financial interests/personal relationships which may be considered as potential competing interests.

References

1 Y. Guo, F. Gao, J. Xu, Q. Chen, S. Cao and L. Li, *J. Mater. Sci.: Mater. Electron.*, 2018, **29**, 12503–12511.
2 L. Zhou, P. Du, Q. Zhang, J. Zhu, Y. Hou, L. Luo and W. Li, *J. Alloys Compd.*, 2019, **810**, 151897.
3 K. Parida and R. N. P. Choudhary, *J. Mater. Sci.: Mater. Electron.*, 2020, **31**, 13292–13300.
4 W. Wang, G. Yu, R. Wang and C. Jiang, *J. Am. Ceram. Soc.*, 2020, **103**, 432–443.
5 Y. Bai, P. Tofel, J. Palosaari, H. Jantunen and J. Juuti, *Adv. Mater.*, 2017, **29**, 1700767.
6 Y. Han, X. Ren, Z. Sun, L. Li and S. Yu, *J. Mater. Sci.: Mater. Electron.*, 2019, **30**, 15064–15074.
7 T. Maeda, N. Takiguchi, M. Ishikawa, T. Hemsel and T. Morita, *Mater. Lett.*, 2010, **64**, 125–128.
8 Y. Yang, Y. Zhou, J. Ren, Q. Zheng, K. H. Lam and D. Lin, *J. Am. Ceram. Soc.*, 2018, **101**, 2594–2605.
9 V. V. Atuchin, *Nucl. Instrum. Methods Phys. Res., Sect. B*, 2000, **168**, 498–502.
10 R. M. Taziev, *IEEE Trans. Sonics Ultrason.*, 2007, **54**(10), 2060–2069.
11 I. Sh. Steinberg, *et al.*, *Opt. Mater.*, 2018, **78**, 253–258.
12 J. Kreisel, M. Alexe and P. A. Thomas, *Nat. Mater.*, 2012, **11**, 260.
13 T. Chen, J. Meng, S. Wu, J. Pei, Q. Lin, X. Wei, J. Li and Z. Zhang, *J. Alloys Compd.*, 2018, **754**, 184–189.
14 W. Janbua, T. Bongkarn, T. Kolodiazhnyi and N. Vittayakorn, *RSC Adv.*, 2017, **7**, 30166–30176.
15 R. Shi, Y. Pu, W. Wang, X. Guo, J. Li, M. Yang and S. Zhou, *J. Alloys Compd.*, 2020, **815**, 152356.
16 R. Barbosa-Silva, J. F. Silva, U. Rocha, C. Jacinto and C. B. de Araújo, *J. Lumin.*, 2019, **211**, 121–126.
17 A. M. Hamilton, S. ODonnell, B. Zoellner, I. Sullivan and P. A. Maggard, *J. Am. Ceram. Soc*, 2019, **103**(1), 454–464.
18 S. Prasertpalichat and D. P. Cann, *J. Electroceram.*, 2014, **33**, 214–220.
19 Y.-Q. Xu, S.-Y. Wu, L.-N. Wu, C.-C. Ding and L.-J. Zhang, *Int. J. Mod. Phys. B*, 2018, **32**, 1850282.
20 D. Zhang, J. Cheng, F. Shi, Z. Cheng, X. Yang and M. Cao, *RSC Adv.*, 2015, **5**, 33001–33007.
21 Q. Liu, L. Zhang, Y. Chai and W.-L. Dai, *J. Phys. Chem. C*, 2017, **121**, 25898–25907.
22 S. Khemakhem, S. Yahyaoui, R. Ben Hassen, H. Khemakhem and A. Ben Salah, *Solid State Sci.*, 2003, **5**, 367–371.
23 Y. D. Juang, S. B. Dai, Y. C. Wang, J. S. Hwang, M. L. Hu and W. S. Tse, *J. Appl. Phys.*, 2000, **88**, 742–745.
24 H. Khelifi, A. Aydi, N. Abdelmoula, A. Simon, A. Maalej, H. Khemakhem and M. Maglione, *J. Mater. Sci.*, 2012, **47**, 1943–1949.
25 S. K. Mohanty, H. S. Mohanty, B. Behera, D. P. Datta, S. Behera and P. R. Das, *J. Mater. Sci.: Mater. Electron.*, 2019, **30**, 5833–5844.

26 X. B. Wang, Z. X. Shen, Z. P. Hu, L. Qin, S. H. Tang and M. H. Kuok, *J. Mol. Struct.*, 1996, **385**, 1–6.
27 N. Baskaran and H. Chang, *Mater. Chem. Phys.*, 2003, **77**, 889–894.
28 H. M. Rietveld, *J. Appl. Crystallogr.*, 1969, **2**, 65–71.
29 W. Beskow and V. M. Goldschmidt, *Geologiska Föreningen i Stockholm Förhandlingar*, 1924, **46**(6–7), 738–743.
30 A. Bauzá, T. J. Mooibroek and A. Frontera, *CrystEngComm*, 2016, **18**, 10–23.
31 H. Slimi, A. Oueslati and A. Aydi, *Appl. Phys. A*, 2019, **510**, 1–10.
32 M. Boukriba, F. Sediri and N. Gharbi, *Mater. Res. Bull.*, 2013, **48**, 574–580.
33 I. Zouari, Z. Sassi, L. Seveyrat, V. Perrin, S. Zghal, N. Abdelmoula, L. Lebrun and H. Khemakhem, *J. Electron. Mater.*, 2017, **46**, 4662–4669.
34 F. Kang, L. Zhang, B. Huang, P. Mao, Z. Wang, Q. Sun, J. Wang and D. Hu, *J. Eur. Ceram. Soc.*, 2020, **40**, 1198–1204.
35 A. Simon, J. Ravez and M. Maglione, *J. Phys.: Condens. Matter*, 2004, **16**, 963–970.
36 Y. Han, X. Ren, Z. Sun, L. Li and S. Yu, *J. Mater. Sci.: Mater. Electron.*, 2019, **30**, 15064–15074.
37 R. Roukos, J. Romanos, S. A. Dargham and D. Chaumont, *J. Eur. Ceram. Soc.*, 2019, **39**, 2297–2303.
38 J. Ma, X. Liu, C. Zhou, C. Yuan, W. Li and M. Jiang, *Ceram. Int.*, 2014, **40**, 2979–2984.
39 K. Uchino and S. Nomura, *Ferroelectrics*, 1982, **44**, 55–61.
40 Z. Raddaoui, S. El Kossi, J. Dhahri, N. Abdelmoula and K. Taibi, *RSC Adv.*, 2019, **9**, 2412–2425.
41 J. Hao, Z. Xu, R. Chu, W. Li, G. Li and Q. Yin, *J. Alloys Compd.*, 2009, **484**, 233–238.
42 K. Hao, W. Ge, Z. Ren, X. Liu, L. Luo, X. Li, H. Luo and D. Viehland, *J. Am. Ceram. Soc.*, 2020, **103**, 3349–3360.
43 S. Aydi, A. Amouri, S. Chkoundali and A. Aydi, *Ceram. Int.*, 2017, **43**, 12179–12185.
44 S. Li, Y.-H. Lin, B.-P. Zhang, Y. Wang and C.-W. Nan, *J. Phys. Chem. C*, 2010, **114**, 2903–2908.
45 W. Ben Nasr, A. Mahmoud, F. Boschini and A. Ben Rhaiem, *J. Alloys Compd.*, 2019, **788**, 522–532.
46 A. K. Sinha, B. Bhushan, J. Jagannath, R. K. Sharma, S. Sen, B. P. Mandal, S. S. Meena, P. Bhatt, C. L. Prajapat, A. Priyam, S. K. Mishra and S. C. Gadkari, *Results Phys.*, 2019, **13**, 102299.
47 Z. Wang, H. Gu, Y. Hu, K. Yang, M. Hu, D. Zhou and J. Guan, *CrystEngComm*, 2010, **12**, 3157.
48 S. A. Ansari, A. Nisar, B. Fatma, W. Khan and A. H. Naqvi, *Mater. Sci. Eng., B*, 2012, **177**, 428–435.
49 R. Jeevan Kumar and D. Kothandan, *Int. J. ChemTech Res.*, 2015, **8**, 410–314.
50 V. Kumar and S. Singh, *J. Alloys Compd.*, 2018, **732**, 350–357.
51 B. Bhushan, A. Basumallick, N. Y. Vasanthacharya, S. Kumar and D. Das, *Solid State Sci.*, 2010, **12**, 1063–1069.
52 R. Lefi, F. Ben Naser and H. Guermazi, *J. Alloys Compd.*, 2017, **696**, 1244–1254.